Quantifying Charge Carrier Recombination Losses in $MAPbI_3$/C60 and $MAPbI_3$/Spiro-OMeTAD with and without Bias Illumination

Caselli, V. M.; Savenije, T. J.

DOI
10.1021/acs.jpclett.2c01728

Publication date
2022

Document Version
Final published version

Published in
Journal of Physical Chemistry Letters

THE JOURNAL OF PHYSICAL CHEMISTRY LETTERS
A JOURNAL OF THE AMERICAN CHEMICAL SOCIETY

pubs.acs.org/JPCL

Letter

Quantifying Charge Carrier Recombination Losses in $MAPbI_3$/C60 and $MAPbI_3$/Spiro-OMeTAD with and without Bias Illumination

V.M. Caselli and T.J. Savenije*

Cite This: *J. Phys. Chem. Lett.* 2022, 13, 7523−7531

Read Online

ACCESS | Metrics & More | Article Recommendations | Supporting Information

ABSTRACT: To increase the open-circuit voltage in perovskite-based solar cells, recombination processes at the interface with transport layers (TLs) should be identified and reduced. We investigated the charge carrier dynamics in bilayers of methylammonium lead iodide ($MAPbI_3$) with C60 or Spiro-OMeTAD using time-resolved microwave conductance (TRMC) measurements with and without bias illumination (BI). By modeling the results, we quantified recombination losses in bare $MAPbI_3$ and extraction into the TLs. Only under BI did we find that the density of deep traps increases in bare $MAPbI_3$, substantially enhancing trap-mediated losses. This reversible process is prevented in a bilayer with C60 but not with Spiro-OMeTAD. While under BI extraction rates reduce significantly in both bilayers, only in $MAPbI_3$/Spiro-OMeTAD does interfacial recombination also increases, substantially reducing the quasi Fermi level splitting. This work demonstrates the impact of BI on charge dynamics and shows that adjusting the Fermi level of TLs is imperative to reduce interfacial recombination losses.

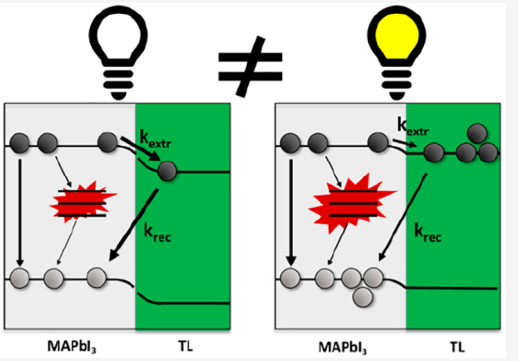

Metal halide perovskite-based solar cells (PSCs) have improved significantly over the past years, reaching device efficiencies over 25%.[1] This impressive progress can be attributed to different optimization procedures. The perovskite layer properties have been perfected by optimizing the synthesis and deposition methods to obtain more stable and highly crystalline perovskite layers.[1−4] At the device level, many approaches have been proposed to improve the interface properties between the perovskite absorber layer and the selective transport layers (TLs).[5] Poor band alignment, defect states at the interfaces, and instability of the used transport materials lead to a reduction in device performance, typically in the form of a reduction of the open-circuit voltage (V_{oc}).[6] To overcome these issues, many different materials, organic and inorganic, have been examined as electron or hole transport layers.[7−11] However, for rational design of efficient perovskite-based solar cells with a high V_{oc}, it is essential to obtain information regarding the rates for the charge extraction and recombination processes occurring at the perovskite/TL interfaces.

Different experimental methods have been used to characterize the interface of the perovskite layer with the TLs.[5,8,12,13] Increasing photoluminescence yields and enhanced device stabilities and efficiencies have been often related to improved interfacial properties. Nonetheless, only a few research groups have been able to provide a quantitative analysis of the rate constants for charge extraction and interfacial recombination.[14−19] In all these studies, the charge carrier dynamics have been investigated by means of time-resolved techniques using pulsed illumination sources. However, the kinetic parameters that can be extracted from a time-resolved analysis are not always representative of the dynamics under steady-state illumination.[20] In addition, it has been reported that, for example, $MAPbI_3$ is unstable under continuous illumination. More specifically, ion migration has been found to be the cause of several instability issues and hysteresis in the $J-V$ curves of $MAPbI_3$-based devices.[5,7,9,21] It can be expected that ion migration influences not only the charge carrier dynamics in the perovskite layer but also the efficiency of the charge extraction process by the TLs.[7,22] For these reasons, quantitatively studying the charge carrier extraction in perovskite/TL bilayers under steady-state illumination is relevant to fully characterize the interfacial processes.

In this Letter we provide a quantitative analysis to extract the rates of charge carrier extraction and recombination processes for methylammonium lead iodide ($MAPbI_3$) with selective TLs (see Scheme 1) under bias illumination (BI). C60 and Spiro-OMeTAD are chosen as electron transport layer (ETL) and hole transport layer (HTL), respectively, as they are the most commonly applied materials in the corresponding p-i-n and n-i-p cell structures. The dynamics

Received: June 7, 2022
Accepted: August 9, 2022
Published: August 10, 2022

Scheme 1. (a) Schematic Representation of a $MAPbI_3$/ETL Heterojunction and Relevant Kinetic Processes Occurring under Illumination; (b) Schematic Representation of the Sample Configuration and Excitation Side[a]

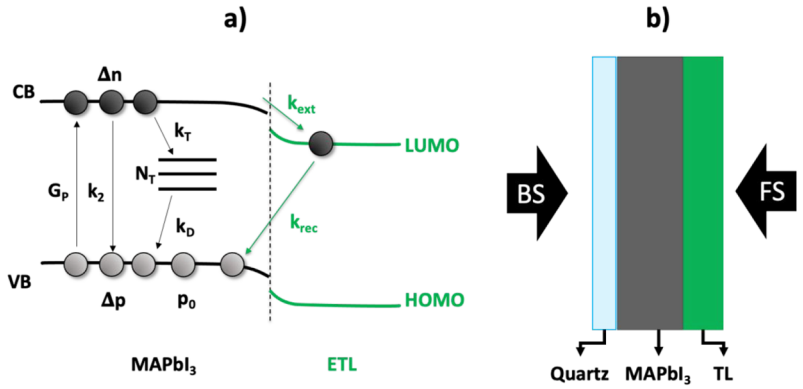

[a]In panel a, the processes in the $MAPbI_3$ film are shown in black, while the charge carrier extraction and back recombination due to the presence of the ETL are shown in green. In panel b, front side (FS) is performed by illuminating the sample from the perovskite/TL side, back side (BS) excitation by illuminating though the quartz substrate

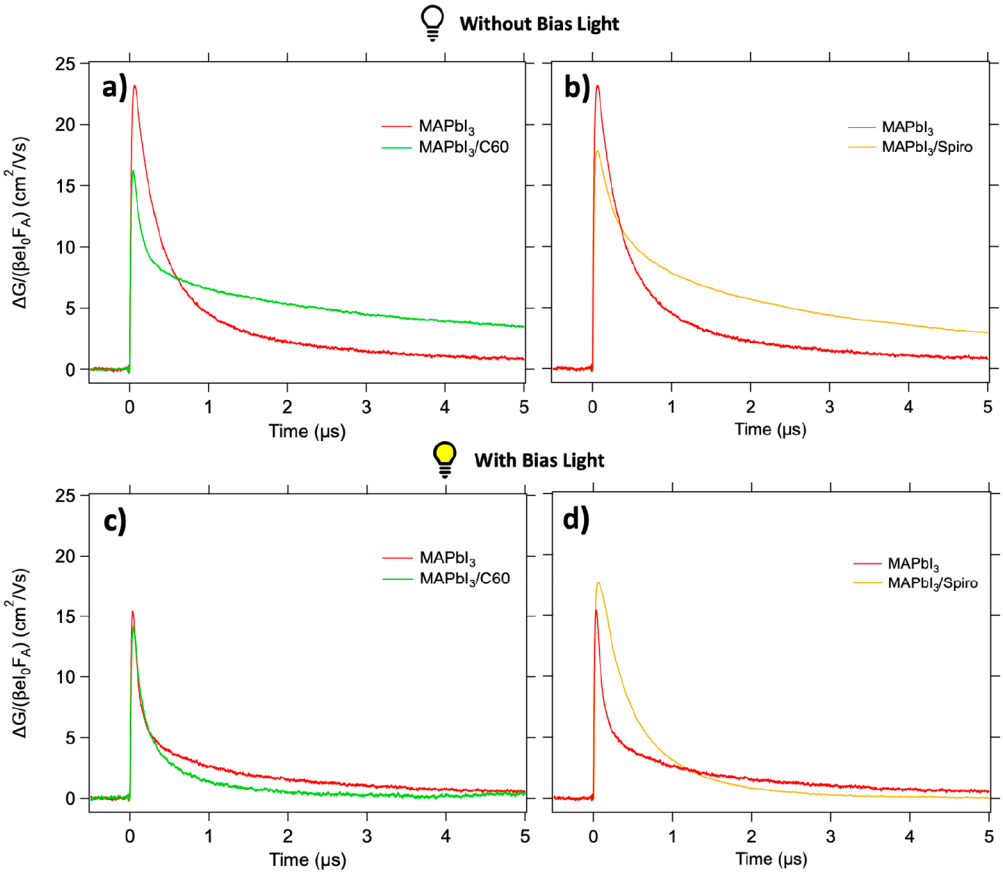

Figure 1. TRMC results upon excitation at 650 nm yielding an initial excitation density of 10^{15} charges/cm^3/pulse for $MAPbI_3$ (red), $MAPbI_3$/C60 (green), and $MAPbI_3$/Spiro-OMeTAD (orange) in absence (a and b) and presence (c and d) of a 0.3 sun bias illumination.

are revealed by time-resolved microwave photoconductance (TRMC) measurements in the presence or absence of continuous bias illumination with an intensity comparable to 0.3 suns. The analysis has been carried out by first investigating the optoelectronic properties of the bare $MAPbI_3$ layer, followed by the $MAPbI_3$/C60 and $MAPbI_3$/Spiro-OMeTAD bilayers. The contactless TRMC measurements are performed over a broad intensity range from 10^{13}–10^{15} cm^{-3}, allowing us to quantify the various rate constants (see Scheme 1a). Unless specified otherwise, the samples have been illuminated from the quartz side, referred to as the back side (BS) in Scheme 1b, in order to reduce parasitic absorption of BI by the TLs.

Confirming previous findings, we observe in $MAPbI_3$/C60 bilayers fast and efficient charge extraction by the C60 layer on pulsed illumination.[8−10,23] However, while a bare $MAPbI_3$ layer shows fully reversible degradation under BI, the introduction of C60 suppresses this degradation process. On the other hand, the $MAPbI_3$/Spiro-OMeTAD bilayer is

https://doi.org/10.1021/acs.jpclett.2c01728
J. Phys. Chem. Lett. 2022, 13, 7523−7531

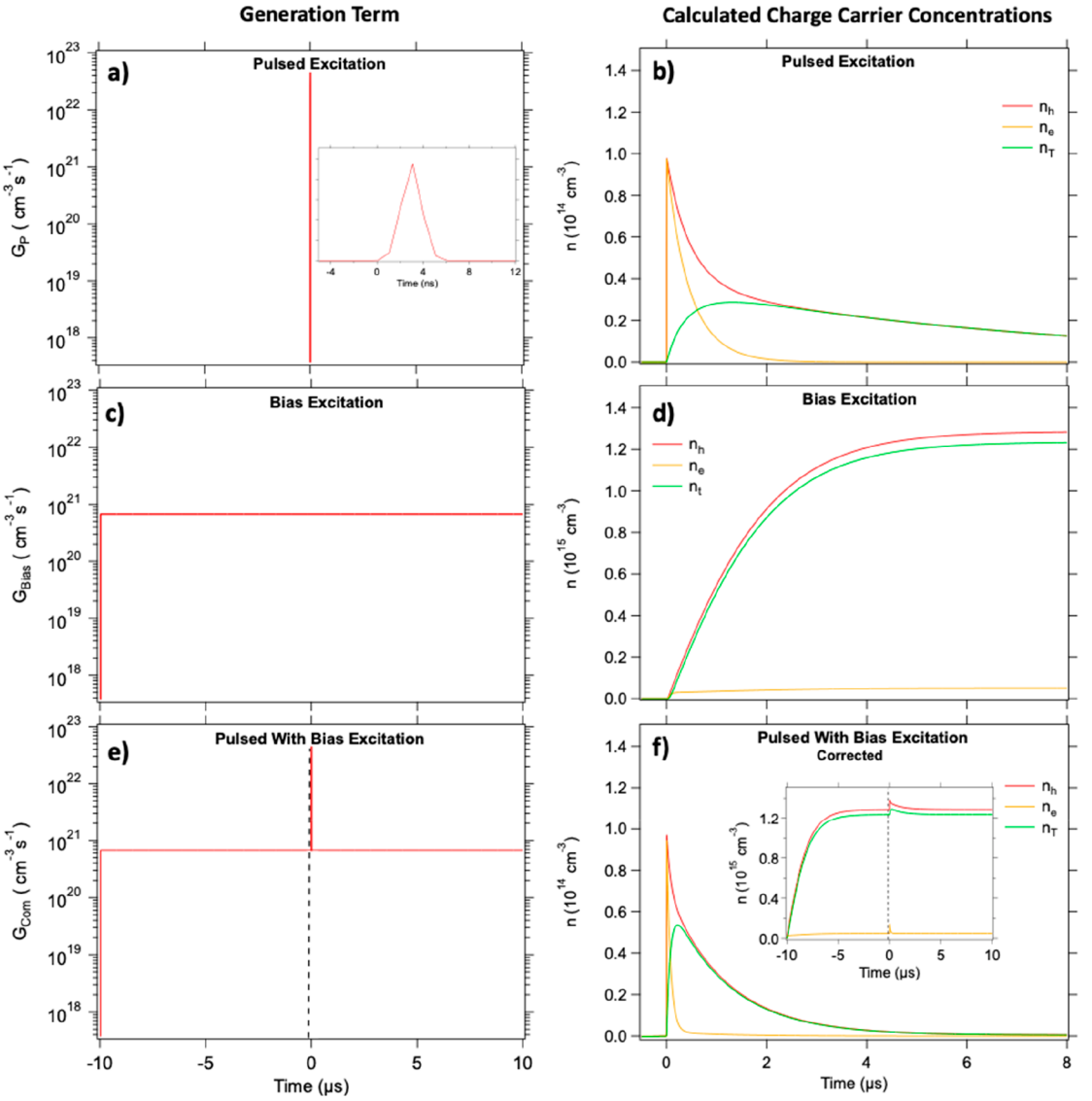

Figure 2. Simulation of the charge carrier concentrations using different illumination sources for a bare $MAPbI_3$ layer. When only pulsed excitation is used, the generation term, G_P, represents the temporal generation profile of the laser pulse and its intensity (here 9.8×10^{13} charges/cm^3 per pulse) shown in panel a, which results in the electron (orange), hole (red), and trapped carrier (green) concentrations shown in panel b. The steady-state concentrations can be modeled with a continuous generation profile, as represented in panel c, leading to the modeled concentrations shown in panel d. For the analysis of the TRMC traces in the presence of bias illumination, the two generation terms are combined to G_{Com} as shown in panel e. After subtraction of the DC contribution, we can extract the relevant concentrations, as presented in panel f. The magnitude of G_{Bias} for the bias illumination is derived from the LED power as described in the Supporting Information.

characterized by the formation of an internal electric field affecting the charge extraction. Furthermore, under BI the concentration defect states at the $MAPbI_3$/Spiro-OMeTAD interface increases substantially, which leads to partially irreversible changes in charge carrier dynamics. Finally, we calculate the concentrations of carriers under BI using the found kinetic parameters extracted from the TRMC analysis.[24] From these concentrations, quantification of the recombination losses and the quasi Fermi level splitting corresponding to the upper limit of qV_{OC} of a device are determined and discussed.

$MAPbI_3$ thin films have been spin-coated onto quartz substrates following a previously reported procedure.[23] Optical and morphological characterizations are reported in the Supporting Information. A 30 nm thick C60 layer has been added via physical vapor deposition, while Spiro-OMeTAD has been spin-coated on top of the $MAPbI_3$ film, as described in the Supporting Information. First, the TRMC signals observed upon 650 nm photoexcitation of single and bilayers of $MAPbI_3$ (red) and $MAPbI_3$/TL (with ETL in green and HTL in orange) without BI are shown in Figure 1a,b. Two characteristics can be observed: the magnitude of the TRMC signal of the bilayers is reduced with respect to the signal of the bare $MAPbI_3$, and at the same time, part of the photoconductance signal shows a slower decay.[23] The present results are in qualitative agreement with the data on single and double layers reported previously.[23] Both these effects can be explained by efficient charge carrier extraction by the TLs. Basically, the TRMC signal is proportional to the concentration of charge carriers, n_i, times their mobility, μ_i, as given in eq 1:

$$\Delta G(t) = e\beta L \sum n_i(t)\mu_i \quad (1)$$

https://doi.org/10.1021/acs.jpclett.2c01728
J. Phys. Chem. Lett. 2022, 13, 7523−7531

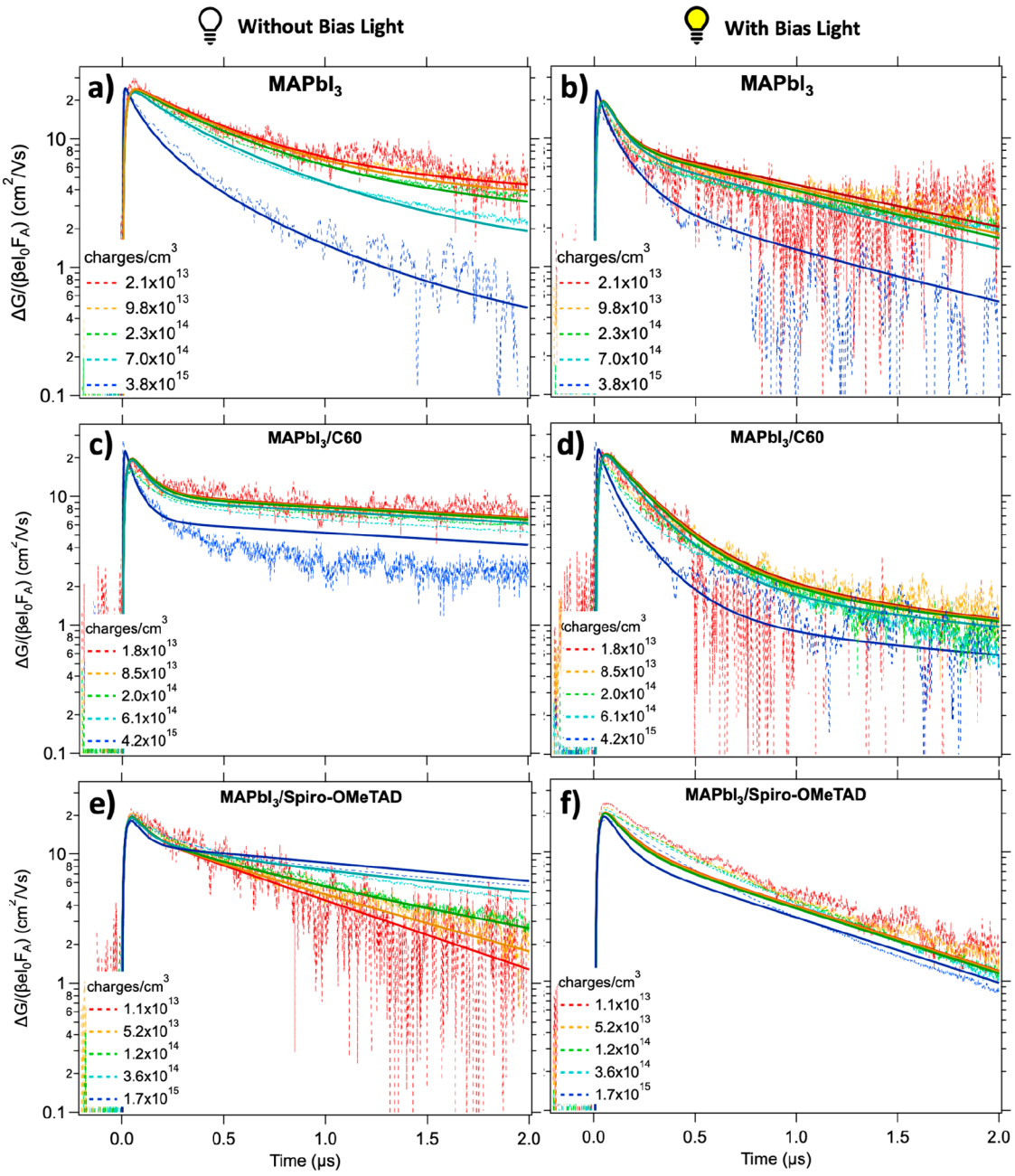

Figure 3. TRMC traces (dashed lines) and fits (solid lines) upon 650 nm pulsed excitation without (left) and with (right) bias illumination for $MAPbI_3$ single layer (a and b), $MAPbI_3$/C60 (c and d), and $MAPbI_3$/Spiro-OMeTAD (e and f).

Here, e is the elementary charge, β a dimensionality factor, and L the sample thickness. As the electron and hole mobilities in the TLs are more than 1 order of magnitude lower than in the perovskite layer, the extracted carriers have a negligible contribution to the measured photoconductance signal.[25,26] This results in lower signals for the bilayers compared to the bare $MAPbI_3$ layer. Furthermore, if efficient extraction occurs, the charge concentration of one type of carrier in the bands is less, reducing the decay by (non) radiative second-order recombination, and thus, long-lived photoconductance signals are observed.

The TRMC results obtained under BI are shown in Figure 1c,d, displaying overall faster decays. This is expected because the higher excess charge carrier concentrations under BI enhance second-order recombination. Most interestingly, the dynamics in the $MAPbI_3$/C60 bilayer is almost identical to that in the $MAPbI_3$ single layer, as is evident from Figure 1c, suggesting reduced charge extraction. Also, for the $MAPbI_3$/Spiro-OMeTAD bilayer, faster decays are observed on BI and the decay does not show any long-lived tail. Nonetheless, in comparison to the single $MAPbI_3$ layer under BI, the lifetimes for the bilayer are still substantially longer (see Figure 1d). This might imply that part of the excess carriers is still extracted by the Spiro-OMeTAD, although less extensively than without BI. As shown in Figure S5, similar trends can be observed upon FS excitation of the bilayers. The independence of the excitation side implies that neither the initial excitation profile nor the period involved with diffusion of charges through the $MAPbI_3$ dominates the decay kinetics on the used time scales.

https://doi.org/10.1021/acs.jpclett.2c01728
J. Phys. Chem. Lett. 2022, 13, 7523−7531

Table 1. Rate Constants and Trap Densities Used for the Fits to the TRMC Signals of Bare $MAPbI_3$, $MAPbI_3$/C60, and $MAPbI_3$/Spiro-OMeTAD without and with Bias Illumination

	without bias			with bias		
	$MAPbI_3$	$MAPbI_3$/C60	$MAPbI_3$/ Spiro	$MAPbI_3$	$MAPbI_3$/ C60	$MAPbI_3$/ Spiro
k_2 ($\times 10^{-9}$ cm^3/s)	2.0	2.0	1.8	2.0	2.0	1.8
k_T ($\times 10^{-9}$ cm^3/s)	9.8	9.8	9.8	9.8	9.8	9.8
k_D ($\times 10^{-9}$ cm^3/s)	0.20	0.20	0.20	0.20	0.20	0.20
N_T ($\times 10^{14}$ cm^{-3})	1.0	1.0	1.0	22	3.0	22
p_0 ($\times 10^{14}$ cm^{-3})	6.5	6.5	0.6	6.5	6.5	0.6
k_{ext} ($\times 10^6$ cm^3/s^{-1})		9.0	15		1.0	8.0
k_{rec} ($\times 10^6$ cm^3/s^{-1})		0.20	0.23		0.20	1.0

In order to deduce the charge carrier extraction rates with and without BI, we adapted the kinetic model presented by Hutter et al.[27] The model accounts for all the processes provided in Scheme 1a, and it allows us to determine the time-dependent charge carrier concentrations by solving four coupled differential eqs (eqs 2−5 for perovskite/ETL heterojunctions, and equations S2−S5 in the Supporting Information for a perovskite/HTL bilayer).

$$\frac{dn_e}{dt} = G_P - k_2 n_e(n_h + p_0) - k_T n_e(N_T - n_T) - k_{ext} n_e \quad (2)$$

$$\frac{dn_h}{dt} = G_P - k_2 n_e(n_h + p_0) - k_D n_t(n_h + p_0) - k_{rec} n_h \quad (3)$$

$$\frac{dn_T}{dt} = k_T n_e(N_T - n_T) - k_D n_T(n_h + p_0) \quad (4)$$

$$\frac{dn_{ETL}}{dt} = k_{ext} n_e - k_{rec} n_h \quad (5)$$

These equations include generation and recombination terms for electrons, n_e, and holes, n_h. G_P is the pulsed generation term; k_2 is the second-order rate constant; and k_T and k_D are the trapping and detrapping rate constants, respectively. It is important to note that the second-order recombination revealed by TRMC measurements accounts for both radiative and nonradiative contributions, as discussed in a previous study.[28] These parameters, together with the total number of trap states, N_T, and background carrier concentration, p_0, are characteristic of spin-coated $MAPbI_3$. Because of the p-type character of $MAPbI_3$, n_0 is negligible, and this term is left out in the coupled differential equations. Charge carrier extraction is characterized by the extraction and back recombination rate constants, k_{ext} and k_{rec}, respectively.

Typically, TRMC results are modeled taking into account the temporal laser pulse profile and its intensity (Figure 2a), resulting in the G_P term used in eqs 2 and 3. The modeled photoconductance signals, fits to the TRMC traces, result from the sum of the time-dependent electron and hole contributions times their individual mobilities at specific intensities. In Figure 2b, the modeled electron (orange), hole (red), and trapped electron (green) concentrations are shown for the specific case of 9.8×10^{13} excitations/cm^3/pulse of the bare $MAPbI_3$ layer. In the next step we use the kinetic parameters obtained from the TRMC analysis to model the concentration of electrons and holes in the perovskite material under BI.[24] This is achieved by replacing the temporal profile of the laser pulse with a continuous illumination profile, G_{Bias} as shown in Figure 2c (see the Supporting Information for calculation of G_{Bias}). The results for the $MAPbI_3$ single layer, presented in Figure 2d, show that an equilibrium is reached in the perovskite film within 6 μs, after which electron and hole concentrations remain constant. In order to model the laser pulse-induced TRMC traces under BI, both the continuous bias illumination and laser pulse are combined in the generation term, G_{Com}, as shown in Figure 2e. The calculated concentration profiles from the model are shown in the inset of Figure 2f. Since the TRMC setup records only the AC part of the photoconductance, the modeled traces are vertically shifted, providing only the AC contributions as exemplified in Figure 2f (see Experimental Methods for details) These calculated traces show the characteristic decays of a pulsed laser experiment but take into account the charge carrier concentrations induced by the BI.

The above model and fitting procedure were applied to the three systems under investigation, i.e., bare $MAPbI_3$, $MAPbI_3$/C60, and $MAPbI_3$/Spiro-OMeTAD for many laser intensities. The protocol to obtain values for the various parameters by fitting the TRMC traces is described in the Supporting Information. The TRMC results (dashed lines) and corresponding fits (solid lines) are shown in Figure 3, while the kinetic parameters are reported in Table 1. The iterative and global analysis of the three systems in parallel allows a detailed and accurate quantification of the optoelectronic properties of $MAPbI_3$. The fact that the excitation profile and corresponding charge diffusion within the $MAPbI_3$ have no effect on the TRMC signal justifies the use of homogeneous differential equations on a clearly nonhomogeneous system. Electron and hole mobilities in $MAPbI_3$ were found to be 30 and 25 cm^2/(Vs), respectively, in agreement with previously reported values.[24] Furthermore, in the absence of BI, the results revealed the presence of 10^{14} cm^{-3} deep trap states, N_T, in bare $MAPbI_3$, while the dark carrier concentration, p_0, was found to be 6.5×10^{14} cm^{-3} (Figure 3a and Table 1). For laser intensities yielding an excess charge density < N_T, the traces overlap, while for higher intensities, second-order recombination becomes the dominant factor in the decay kinetics.

Interestingly, we observed a strong reduction of p_0 to a value of 6.0×10^{13} cm^{-3} in the $MAPbI_3$/Spiro-OMeTAD bilayer (Figure 3e), while for $MAPbI_3$/C60 no change in p_0 was observed. This can be explained by assuming that the Fermi level of the $MAPbI_3$ is below that of Spiro-OMeTAD. Note that the Spiro-OMeTAD in this study was not intentionally doped nor exposed to oxygen. Equilibration of the Fermi levels on contacting $MAPbI_3$ and Spiro-OMeTAD leads to transfer of positive carriers to the latter. This implies that our bare $MAPbI_3$ layer deposited on quartz is to some extent p-doped, which is in line with recent studies.[29,30] To corroborate this explanation, we performed steady-state microwave conduc-

https://doi.org/10.1021/acs.jpclett.2c01728
J. Phys. Chem. Lett. 2022, 13, 7523−7531

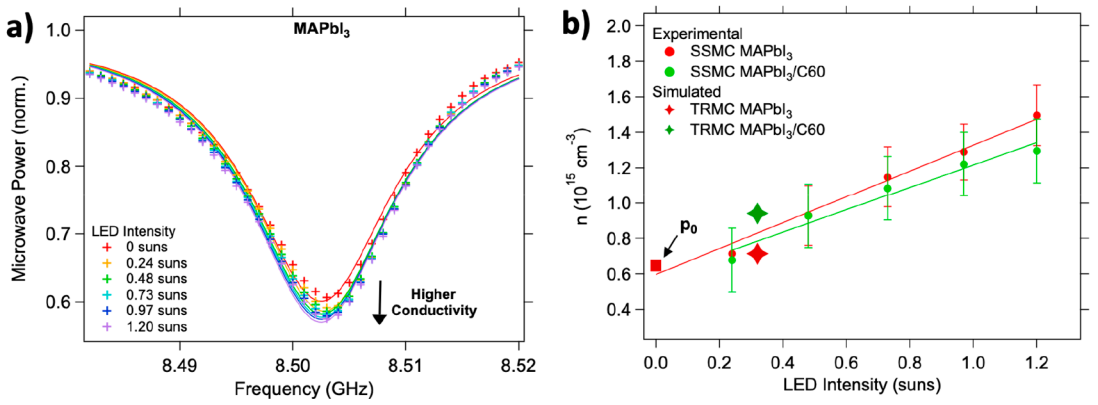

Figure 4. (a) Evolution of the steady-state microwave conductance dip under various LED light intensity values. The experimental data points are indicated by the markers. The solid lines represent the fits from which the conductivity and corresponding carrier concentrations have been derived. A decrease of the normalized microwave power is related to an increased conductivity in the sample, i.e., higher charge carrier concentration under illumination. (b) Charge carrier concentrations in $MAPbI_3$ (red) and $MAPbI_3$/C60 (green) experimentally determined by SSMC measurements (circles) are compared to the simulated concentrations at 0.3 suns (diamonds), showing excellent agreement. The background concentration of charge carriers, p_0, determined from the fits is also shown as a red square at the LED intensity of 0 suns.

tance (SSMC) measurements on bare and bilayers in the dark. An SSMC experiment provides information on the background conductivity of a semiconductor layer.[31] On comparison of the $MAPbI_3$ to the $MAPbI_3$/Spiro-OMeTAD bilayer, we observed an appreciable reduction of the background conductivity in the bilayer (see the Supporting Information, Figure S4). In analogy to the reasoning above on equilibration of the Fermi levels, holes are transferred from the $MAPbI_3$ to the Spiro-OMeTAD layer. Because of the decreased hole mobility in the Spiro-OMeTAD, an overall reduction in conductivity is expected in agreement with our SSMC experiments. This result supports the conclusion regarding the type of doping in $MAPbI_3$. Apart from this change in p_0 for the $MAPbI_3$/Spiro-OMeTAD bilayer, we can use for fitting the bilayers the kinetic parameters found for the $MAPbI_3$ layer completed by introduction of a first-order extraction and a recombination process (see Table 1). Interestingly the presented kinetic model captures the reversed intensity dependencies for both bilayers very well (compare panels c and e of Figure 3). For the $MAPbI_3$/Spiro-OMeTAD, a higher intensity leads to longer lifetimes, while for the $MAPbI_3$/C60, higher intensities lead to faster decays. As previously discussed,[23,27] the different behaviors are related to the nature of the deep trap states in $MAPbI_3$, which have been proven to be electron traps.

Now we turn to the experiments with BI and start with the bare $MAPbI_3$ shown in Figure 1c. The fast recombination is followed by a small but long-lived tail. Fits on the TRMC signals with BI (Figure 3b) reveal that, most importantly, the same parameters can be used except for the trap state concentration, N_T, which increases by more than 1 order of magnitude, reaching 22×10^{14} cm^{-3}. This increment can be related to ionic motion in the $MAPbI_3$ film, induced by the BI. Interestingly after storage of the $MAPbI_3$ film in the dark for 3 h, N_T reverts back to its original value, which demonstrates the reversibility of this degradation process (see Figure S7a in the Supporting Information). Taking this light instability into account, the model can accurately fit the TRMC traces without any further modification of the fitting parameters given in Table 1, as can be seen from Figure 3b.

As mentioned, BI of the $MAPbI_3$/C60 bilayer leads to decay kinetics comparable to those of $MAPbI_3$ under BI. However, the $MAPbI_3$/C60 bilayer does not show any sign of a tail (see Figure 2c) implying no major increase in N_T under BI; that is, N_T does not substantially vary in strong contrast with the value found in bare $MAPbI_3$. In fact, from the fitting of the TRMC traces of the $MAPbI_3$/C60 bilayer with BI, we observe only a minor increment of the trap state concentration, reaching 3×10^{14} cm^{-3}. Hence, we can conclude that the C60 layer hinders the formation of additional deep trap states under BI, presumably at the surface of the $MAPbI_3$. This is in line with previous research arguing that C60 is able to passivate the surface of perovskite materials, resulting in efficient charge carrier extraction and high device efficiencies.[8−10,23] From Table 1 we notice that the only parameter that changes under BI is k_{ext}. We suggest that k_{ext} is reduced under BI because of pilling up of electrons in the C60. This leads to formation of an electric field over the interface, impeding the extraction process of electrons into C60.

For the $MAPbI_3$/Spiro-OMeTAD bilayer measured under BI, a combination of both effects is observed. In contrast to $MAPbI_3$/C60 bilayers, the presence of Spiro-OMeTAD does not prevent the degradation process leading to an increase of N_T. Furthermore, the extraction process is reduced by the presence of the bias illumination, in combination with a 4-fold increase of k_{rec} (see Table 1). As previously mentioned, the instability of $MAPbI_3$ under BI can be related to ionic motion in the perovskite layer. During BI of the $MAPbI_3$/Spiro-OMeTAD bilayer, holes are collected and accumulate in the HTL, attracting negatively charged iodine ions toward the interface. Ion accumulation at the interface has been indicated as one of the reasons of hysteresis in the $J-V$ curves[5,7,9,21] and could explain the changes in extraction (reduced) and interfacial recombination (increased) rate constants. In addition, TRMC measurements performed after the BI was turned off showed much faster decay kinetics, which only partially recovered after 24 h, as shown in Figure S7c. It has been reported that some of the iodine ions can chemically interact with the Spiro-OMeTAD molecule, leading to irreversible degradation of the HTL,[18] in line with the only partial recovery that we observe. The results presented here provide a strong link between the surface/interface properties

https://doi.org/10.1021/acs.jpclett.2c01728
J. Phys. Chem. Lett. 2022, 13, 7523−7531

Table 2. Calculated Loss Fractions Using the Kinetic Parameters from the TRMC Fits at 0.3 suns[a]

	second order (%)	trap-assisted (%)	charge extraction (%)	populated N_T (%)	QFLS (eV)
$MAPbI_3$	29 (97)	71 (3)		56 (93)	1.12 (1.16)
$MAPbI_3$/C60	54 (36)	11 (3.5)	23 (60.5)	84 (45)	1.15 (1.13)
$MAPbI_3$/Spiro	16 (40)	8 (0.30)	75 (59.7)	99 (100)	1.11 (1.13)

[a]The values are obtained using the "with bias" fitting parameters of Table 1. The values in parentheses are obtained using the "without bias" parameters and are provided for comparison.

and the instability of the perovskite under steady-state illumination.

Although the model presented in Scheme 1 might not include all processes in full detail, the combined set of processes can be used to describe the main trends of the charge carrier dynamics in $MAPbI_3$ and bilayers under BI. Knowing the rate constants enables us to calculate a number of interesting aspects, including the various loss factors and the quasi Fermi level splitting (QFLS) under simulated sun light. We calculated the steady-state carrier concentrations described by the coupled differential equations. The generation term, G_{Bias}, comprises the intensity corresponding to illumination of the $MAPbI_3$ layer with 0.3 suns (see the Supporting Information for the calculation). The evolution of the various concentrations in time until steady-state is achieved is shown in Figures S6. Furthermore, the calculated concentrations are compared to the results of the SSMC experiments for $MAPbI_3$ and $MAPbI_3$/C60 samples (see Figure 4a for $MAPbI_3$ data). From the fits (solid lines) to the data points (markers) the concentration of charge carriers as a function of the light intensity can be derived (see Figure 4b).[24,32] The SSMC results on $MAPbI_3$/Spiro-OMeTAD have not been included because of the light instability of the bilayer at higher illumination densities. In Figured 4b, these SSMC results are compared with the calculated concentrations of mobile charges at 0.3 suns, showing perfect agreement. However, the calculated values at 1 sun are a factor of 2−3 too high, exceeding 2.0×10^{15} cm^{-3} in $MAPbI_3$ and 3.0×10^{15} cm^{-3} in the bilayer (data points not shown). For $MAPbI_3$, this can be attributed to the intensity-dependent light degradation, which makes the N_T value extracted at 0.3 suns inaccurate for simulations at higher intensities. In addition, for $MAPbI_3$/C60 it is likely that at higher intensities the extraction and recombination rates become even closer.

In view of the fact that our model can accurately describe the concentrations at 0.3 suns, the losses for each decay channel can now be quantified and are presented in Table 2. For $MAPbI_3$, the decay via trap-mediated recombination is rather large mainly because of the substantial rise in N_T related to the light instability of $MAPbI_3$ and absence of a surface passivating agent. For the $MAPbI_3$/C60 bilayer, we notice that the charge extraction is limited (<25%) and the carriers mainly decay in the $MAPbI_3$ bulk via second-order and trap-assisted recombination. In contrast, hole extraction and back recombination dominates the kinetics in the $MAPbI_3$/Spiro-OMeTAD bilayer. The majority of the light-induced holes (75%) decays by getting first extracted by the Spiro-OMeTAD followed by recombination with excess electrons. Despite the higher concentration of trap states under bias illumination, trap-assisted recombination is relatively small because of the fast saturation of almost all N_T, followed by slow recombination.

From the concentration curves calculated and shown in Figures S6, also the quasi Fermi level splitting, QFLS, corresponding to the upper limit of qV_{OC} of a device, can be calculated using

$$\mathrm{QFLS} = \frac{kT}{q}\ln\left(\frac{(n_0 + \Delta n)(p_0 + \Delta p)}{n_i^2}\right) \quad (6)$$

In eq 6, k is the Boltzmann constant, T the temperature, and q the elementary charge; n_0 and p_0 represent the thermal equilibrium concentrations of electrons and holes, respectively, while Δn and Δp are the photoexcited excess charge carrier concentrations. The intrinsic carrier concentration, n_i, has been evaluated to be ca. 1×10^5 cm^{-3}. The calculated QFLS values in bare $MAPbI_3$, in $MAPbI_3$/C60, and in $MAPbI_3$/Spiro-OMeTAD bilayers under 0.3 suns are reported in Table 2. A larger splitting is observed in $MAPbI_3$/C60 than for the bare $MAPbI_3$, while a clear reduction is obtained for $MAPbI_3$/Spiro-OMeTAD. This can be expected on the basis of the C60 passivation effect and ionic motion toward the Spiro-OMeTAD interface mentioned in the above discussion. For the latter, reducing the value of k_{rec} is a logical step in order to improve the V_{oc}. Therefore, designing TLs giving rise to an active heterojunction capable of accepting one type and repelling the counter charge is essential. Alternatively, reduction of k_{rec} could be achieved, for example, by introducing an interlayer between the perovskite and TL.[33−36] Furthermore, careful tuning of the band offsets might be a way to influence the rate constants involved.

Lastly, our study reveals that the determination of the kinetic parameters under bias illumination is of utmost importance if we want to understand the loss mechanisms under device operation. Since some of the kinetic parameters are varying with light intensity in $MAPbI_3$ and $MAPbI_3$/TL, these parameters cannot be used for the simulation of device performance directly. As given in parentheses in Table 2, the loss fractions and QFLS values are substantially different in case the "without bias" parameters of Table 1 are used for the steady-state simulation at 0.3 suns. In $MAPbI_3$, the strong underestimation of the trap density would lead to an underestimation of the trap-assisted recombination contribution, ultimately leading to a higher V_{OC}. For the bilayers, the interfacial processes are the most affected by BI. Despite the passivation effect of C60, the electron extraction in $MAPbI_3$/C60 is substantially reduced under BI. For the $MAPbI_3$/Spiro-OMeTAD, the ionic migration toward the interface with Spiro-OMeTAD enhances the interfacial recombination under BI. Moreover, as concluded from the SSMC results, these effects are likely to be even more pronounced at higher illumination intensities.

To summarize, in this Letter we performed time-resolved microwave photoconductance measurements in the presence and absence of bias illumination in single and bilayers. A kinetic model was used to describe the kinetics, including the charge generation and charge recombination and extraction. Owing to the iterative analysis of the three systems using a

https://doi.org/10.1021/acs.jpclett.2c01728
J. Phys. Chem. Lett. 2022, 13, 7523−7531

broad range of laser intensities, we were able to accurately determine the kinetic parameters for bare $MAPbI_3$, $MAPbI_3$/C60, and $MAPbI_3$/Spiro-OMeTAD in the presence and absence of BI. For $MAPbI_3$ we found that the same parameters can be used under BI except for the trap state concentration, N_T, which increases by more than 1 order of magnitude, reaching 22×10^{14} cm^{-3}. This increment is related to ionic motion in the $MAPbI_3$ film. Interestingly, after storage of the $MAPbI_3$ film in the dark for 3 h, N_T reverts back to its original value, which demonstrates the reversibility of this degradation process. For the $MAPbI_3$/C60 bilayer under BI, we observe only a minor increment of N_T, which shows that C60 hinders the formation of additional deep trap states. Under BI, only the extraction rate k_{ext} is reduced because of pilling up of electrons in the C60, which leads to formation of an electric field over the interface, impeding the extraction process of electrons into C60.

In contrast to $MAPbI_3$/C60 bilayers, the presence of Spiro-OMeTAD does not prevent the degradation process leading to an increase of N_T. Furthermore, under BI the extraction process is reduced, in combination with a 4-fold increase of k_{rec}, which are related to ion accumulation at the interface. Moreover, we show that to calculate carrier concentrations for deducing device parameters, like the QFLS, it is important to use the kinetic parameters found under BI, which is in particular relevant for the $MAPbI_3$/Spiro-OMeTAD bilayer. This study adds to the understanding of both the heterojunctions' interfacial properties as well as the origin of the light instability in $MAPbI_3$, crucial factors for the performance of perovskite-based devices.

EXPERIMENTAL METHODS

The TRMC is a contactless technique, whose working principle is based on the interaction of microwaves with photoexcited charge carriers.[37] In a TRMC measurement, the sample is illumined by a short laser pulse (3 ns fwhm, 10 Hz) and the light-induced excess charge carriers absorb a small part of the microwave power resulting in a slight reduction of the reflected microwave power, which is monitored by a sensitive microwave detection system. The DC part of the signal is electronically subtracted using an offset regulator, and the remaining AC signal is amplified by a broadband amplifier (GHz–kHz). The changes in measured microwave power, $\Delta P(t)$, are related to the changes in photoconductance, $\Delta G(t)$, by

$$\frac{\Delta P(t)}{P} = -K\Delta G(t) \tag{7}$$

where K is a predetermined sensitivity factor.[37] The recombination pathways revealed by TRMC are not limited to the radiative recombination observed by commonly applied photoluminescence spectroscopy (PL) nor by higher-order recombination processes as in transient absorption (TA). Furthermore, with a slow repetition rate of 10 Hz, all the charges in the sample have relaxed back to the original state before the next pulse arrives. A similar TRMC analysis was conducted to extract the charge carrier dynamics under continuous illumination using a white LED. With a semi-transparent mirror the sample was simultaneously illuminated with the pulsed laser and the LED. The intensity of the latter was 6.6 mW (ca. 0.3 suns in the visible region), leading to the generation rate of approximately 6.7×10^{20} charges/cm^3 per second. Reproducibility within a single batch of $MAPbI_3$ layers is very good, and variations in signal height and lifetimes are typically less than 20%; between batches prepared using the same equipment, the variations increase but are within 50%.

ASSOCIATED CONTENT

Supporting Information

The Supporting Information is available free of charge at https://pubs.acs.org/doi/10.1021/acs.jpclett.2c01728.

Experimental details regarding sample preparation, bias illumination, the microwave conductance technique, and the modeling and fitting protocols (PDF)

AUTHOR INFORMATION

Corresponding Author

T.J. Savenije − *Department of Chemical Engineering, Delft University of Technology, 2629 HZ Delft, The Netherlands;* orcid.org/0000-0003-1435-9885; Email: T.J.Savenije@tudelft.nl

Author

V.M. Caselli − *Department of Chemical Engineering, Delft University of Technology, 2629 HZ Delft, The Netherlands;* orcid.org/0000-0002-3730-5241

Complete contact information is available at: https://pubs.acs.org/10.1021/acs.jpclett.2c01728

Notes

The authors declare no competing financial interest.

ACKNOWLEDGMENTS

V.M.C. and T.J.S. acknowledge funding from the Dutch Research Council (NWO), Grant Number 739.017.004.

REFERENCES

(1) Jeong, J.; Kim, M.; Seo, J.; Lu, H.; Ahlawat, P.; Mishra, A.; Yang, Y.; Hope, M. A.; Eickemeyer, F. T.; Kim, M.; et al. Pseudo-Halide Anion Engineering for α-FAPbI3 Perovskite Solar Cells. *Nature* **2021**, *592*, 381−385.

(2) Zhao, J.; Caselli, V. M.; Bus, M.; Boshuizen, B.; Savenije, T. J. How Deep Hole Traps Affect the Charge Dynamics and Collection in Bare and Bilayers of Methylammonium Lead Bromide. *ACS Appl. Mater. Interfaces* **2021**, *13*, 16309−16316.

(3) Zhang, W.; Pathak, S.; Sakai, N.; Stergiopoulos, T.; Nayak, P. K.; Noel, N. K.; Haghighirad, A. A.; Burlakov, V. M.; Dequilettes, D. W.; Sadhanala, A.; et al. Enhanced Optoelectronic Quality of Perovskite Thin Films with Hypophosphorous Acid for Planar Heterojunction Solar Cells. *Nat. Commun.* **2015**, *6*, 10030.

(4) Hu, Y.; Hutter, E. M.; Rieder, P.; Grill, I.; Hanisch, J.; Aygüler, M. F.; Hufnagel, A. G.; Handloser, M.; Bein, T.; Hartschuh, A.; et al. Understanding the Role of Cesium and Rubidium Additives in Perovskite Solar Cells: Trap States, Charge Transport, and Recombination. *Adv. Energy Mater.* **2018**, *8*, 1703057.

(5) Chen, J.; Park, N. G. Materials and Methods for Interface Engineering toward Stable and Efficient Perovskite Solar Cells. *ACS Energy Lett.* **2020**, *5*, 2742−2786.

(6) Wolff, C. M.; Caprioglio, P.; Stolterfoht, M.; Neher, D. Nonradiative Recombination in Perovskite Solar Cells: The Role of Interfaces. *Adv. Mater.* **2019**, *31*, 1902762.

(7) Kim, T.; Lim, J.; Song, S. Recent Progress and Challenges of Electron Transport Layers in Organic−Inorganic Perovskite Solar Cells. *Energies* **2020**, *13*, 5572.

(8) Wolff, C. M.; Zu, F.; Paulke, A.; Toro, L. P.; Koch, N.; Neher, D. Reduced Interface-Mediated Recombination for High Open-Circuit Voltages in $CH_3NH_3PbI_3$ Solar Cells. *Adv. Mater.* **2017**, *29*, 1700159.

(9) Shao, Y.; Xiao, Z.; Bi, C.; Yuan, Y.; Huang, J. Origin and Elimination of Photocurrent Hysteresis by Fullerene Passivation in CH3NH3PbI3 Planar Heterojunction Solar Cells. *Nat. Commun.* **2014**, *5*, 5784.
(10) Chen, B.; Rudd, P. N.; Yang, S.; Yuan, Y.; Huang, J. Imperfections and Their Passivation in Halide Perovskite Solar Cells. *Chem. Soc. Rev.* **2019**, *48*, 3842−3867.
(11) Arumugam, G. M.; Karunakaran, S. K.; Liu, C.; Zhang, C.; Guo, F.; Wu, S.; Mai, Y. Inorganic Hole Transport Layers in Inverted Perovskite Solar Cells: A Review. *Nano Sel.* **2021**, *2*, 1081−1116.
(12) Sarritzu, V.; Sestu, N.; Marongiu, D.; Chang, X.; Masi, S.; Rizzo, A.; Colella, S.; Quochi, F.; Saba, M.; Mura, A.; et al. Optical Determination of Shockley-Read-Hall and Interface Recombination Currents in Hybrid Perovskites. *Sci. Rep.* **2017**, *7*, 44629.
(13) Caprioglio, P.; Stolterfoht, M.; Wolff, C. M.; Unold, T.; Rech, B.; Albrecht, S.; Neher, D. On the Relation between the Open-Circuit Voltage and Quasi-Fermi Level Splitting in Efficient Perovskite Solar Cells. *Adv. Energy Mater.* **2019**, *9*, 1901631.
(14) Pydzińska, K.; Karolczak, J.; Kosta, I.; Tena-Zaera, R.; Todinova, A.; Idígoras, J.; Anta, J. A.; Ziółek, M. Determination of Interfacial Charge-Transfer Rate Constants in Perovskite Solar Cells. *ChemSusChem* **2016**, *9*, 1647−1659.
(15) Ponseca, C. S.; Hutter, E. M.; Piatkowski, P.; Cohen, B.; Pascher, T.; Douhal, A.; Yartsev, A.; Sundström, V.; Savenije, T. J. Mechanism of Charge Transfer and Recombination Dynamics in Organo Metal Halide Perovskites and Organic Electrodes, PCBM, and Spiro-OMeTAD: Role of Dark Carriers. *J. Am. Chem. Soc.* **2015**, *137*, 16043−16048.
(16) Makuta, S.; Liu, M.; Endo, M.; Nishimura, H.; Wakamiya, A.; Tachibana, Y. Photo-Excitation Intensity Dependent Electron and Hole Injections from Lead Iodide Perovskite to Nanocrystalline TiO2 and Spiro-OMeTAD. *Chem. Commun.* **2016**, *52*, 673−676.
(17) Piatkowski, P.; Cohen, B.; Ramos, J. F.; Nunzio, D.; Di Nunzio, M. R.; Mohammad K, N.; Grätzel, M.; Ahmad, S.; Nunzio, D.; Douhal, A.; et al. Direct Monitoring of Ultrafast Electron and Hole Dynamics in Perovskite Solar Cells. *Phys. Chem. Chem. Phys.* **2015**, *17*, 14674−14684.
(18) Brauer, J. C.; Lee, Y. H.; Mohammad K, N.; Banerji, N. Ultrafast Charge Carrier Dynamics in CH3NH3PbI3: Evidence for Hot Hole Injection into Spiro-OMeTAD. *J. Mater. Chem. C* **2016**, *4*, 5922−5931.
(19) Levine, I.; Al-Ashouri, A.; Musiienko, A.; Hempel, H.; Magomedov, A.; Drevilkauskaite, A.; Getautis, V.; Menzel, D.; Hinrichs, K.; Unold, T.; et al. Charge Transfer Rates and Electron Trapping at Buried Interfaces of Perovskite Solar Cells. *Joule* **2021**, 2915.
(20) Levine, I.; Gupta, S.; Bera, A.; Ceratti, D.; Hodes, G.; Cahen, D.; Guo, D.; Savenije, T. J.; Ávila, J.; Bolink, H. J. Can We Use Time-Resolved Measurements to Get Steady-State Transport Data for Halide Perovskites? *J. Appl. Phys.* **2018**, *124*, 103103.
(21) Futscher, M. H.; Lee, J. M.; McGovern, L.; Muscarella, L. A.; Wang, T.; Haider, M. I.; Fakharuddin, A.; Schmidt-Mende, L.; Ehrler, B. Quantification of Ion Migration in $CH_3NH_3PbI_3$ Perovskite Solar Cells by Transient Capacitance Measurements. *Mater. Horizons* **2019**, *6*, 1497.
(22) Carrillo, J.; Guerrero, A.; Rahimnejad, S.; Almora, O.; Zarazua, I.; Mas-Marza, E.; Bisquert, J.; Garcia-Belmonte, G. Ionic Reactivity at Contacts and Aging of Methylammonium Lead Triiodide Perovskite Solar Cells. *Adv. Energy Mater.* **2016**, *6*, 1502246.
(23) Caselli, V. M.; Wei, Z.; Ackermans, M. M.; Hutter, E. M.; Ehrler, B.; Savenije, T. J. Charge Carrier Dynamics upon Sub-Bandgap Excitation in Methylammonium Lead Iodide Thin Films: Effects of Urbach Tail, Deep Defects, and Two-Photon Absorption. *ACS Energy Lett.* **2020**, *5*, 3821−3827.
(24) Guo, D.; Caselli, V. M.; Hutter, E. M.; Savenije, T. J. Comparing the Calculated Fermi Level Splitting with the Open Circuit Voltage in Various Perovskite Cells. *ACS Energy Lett.* **2019**, *4*, 855−860.
(25) MacKenzie, R. C. I.; Frost, J. M.; Nelson, J. A Numerical Study of Mobility in Thin Films of Fullerene Derivatives. *J. Chem. Phys.* **2010**, *132*, 064904.
(26) Tiazkis, R.; Paek, S.; Daskeviciene, M.; Malinauskas, T.; Saliba, M.; Nekrasovas, J.; Jankauskas, V.; Ahmad, S.; Getautis, V.; Nazeeruddin, M. K. Methoxydiphenylaminesubstituted Fluorene Derivatives as Hole Transporting Materials: Role of Molecular Interaction on Device Photovoltaic Performance. *Sci. Rep.* **2017**, *7*, 150.
(27) Hutter, E. M.; Hofman, J. J.; Petrus, M. L.; Moes, M.; Abellón, R. D.; Docampo, P.; Savenije, T. J. Charge Transfer from Methylammonium Lead Iodide Perovskite to Organic Transport Materials: Efficiencies, Transfer Rates, and Interfacial Recombination. *Adv. Energy Mater.* **2017**, *7*, 1602349.
(28) Brenes, R.; Guo, D.; Osherov, A.; Noel, N. K.; Eames, C.; Hutter, E. M.; Pathak, S. K.; Niroui, F.; Friend, R. H.; Islam, M. S.; et al. Metal Halide Perovskite Polycrystalline Films Exhibiting Properties of Single. *Crystals. Joule* **2017**, *1*, 155−167.
(29) Olthof, S.; Meerholz, K. Substrate-Dependent Electronic Structure and Film Formation of MAPbI 3 Perovskites. *Sci. Rep.* **2017**, *7*, 40267.
(30) Caputo, M.; Cefarin, N.; Radivo, A.; Demitri, N.; Gigli, L.; Plaisier, J. R.; Panighel, M.; Di Santo, G.; Moretti, S.; Giglia, A.; et al. Electronic Structure of MAPbI3 and MAPbCl3: Importance of Band Alignment. *Sci. Rep.* **2019**, *9*, 15159.
(31) Caselli, V. M.; Fischer, M.; Meggiolaro, D.; Mosconi, E.; De Angelis, F.; Stranks, S. D.; Baumann, A.; Dyakonov, V.; Hutter, E. M.; Savenije, T. J. Charge Carriers Are Not Affected by the Relatively Slow-Rotating Methylammonium Cations in Lead Halide Perovskite Thin Films. *J. Phys. Chem. Lett.* **2019**, *10*, 5128−5134.
(32) Guo, D.; Caselli, V. M.; Hutter, E. M.; Savenije, T. J. Comparing the Calculated Fermi Level Splitting with the Open-Circuit Voltage in Various Perovskite Cells. *ACS Energy Lett.* **2019**, *4*, 855−860.
(33) Bouduban, M. E. F.; Queloz, V. I. E.; Caselli, V. M.; Cho, K. T.; Kirmani, A. R.; Paek, S.; Roldan-Carmona, C.; Richter, L. J.; Moser, J. E.; Savenije, T. J.; et al. Crystal Orientation Drives the Interface Physics at Two/Three-Dimensional Hybrid Perovskites. *J. Phys. Chem. Lett.* **2019**, *10*, 5713−5720.
(34) Zhao, R.; Zhang, K.; Zhu, J.; Xiao, S.; Xiong, W.; Wang, J.; Liu, T.; Xing, G.; Wang, K.; Yang, S.; et al. Surface Passivation of Organometal Halide Perovskites by Atomic Layer Deposition: An Investigation of the Mechanism of Efficient Inverted Planar Solar Cells. *Nanoscale Adv.* **2021**, *3*, 2305−2315.
(35) Li, H.; Tao, L.; Huang, F.; Sun, Q.; Zhao, X.; Han, J.; Shen, Y.; Wang, M. Enhancing Efficiency of Perovskite Solar Cells via Surface Passivation with Graphene Oxide Interlayer. *ACS Appl. Mater. Interfaces* **2017**, *9*, 38967−38976.
(36) Koushik, D.; Verhees, W. J. H.; Kuang, Y.; Veenstra, S.; Zhang, D.; Verheijen, M. A.; Creatore, M.; Schropp, R. E. I. High-Efficiency Humidity-Stable Planar Perovskite Solar Cells Based on Atomic Layer Architecture. *Energy Environ. Sci.* **2017**, *10*, 91−100.
(37) Savenije, T. J.; Guo, D.; Caselli, V. M.; Hutter, E. M. Quantifying Charge-Carrier Mobilities and Recombination Rates in Metal Halide Perovskites from Time-Resolved Microwave Photoconductivity Measurements. *Adv. Energy Mater.* **2020**, *10*, 1903788.

https://doi.org/10.1021/acs.jpclett.2c01728
J. Phys. Chem. Lett. 2022, 13, 7523−7531